Batteries & Supercaps

Research Article
doi.org/10.1002/batt.202500672

Chemistry Europe
European Chemical Societies Publishing

www.batteries-supercaps.org

Mechanistic Insights into Sodium Niobate Surface Coating for Enhanced Cycling Performance of Mn—Cu—Fe-Based Layered Oxides for Sodium-Ion Batteries

Ruochen Xu,* Valeriu Mereacre, Robert Leiter, Vanessa Trouillet, Holger Geßwein, Simon Fleischmann, Anass Benayad, Daria Mikhailova, Helmut Ehrenberg, and Joachim R. Binder*

Spray-dried battery active materials exhibit high specific surface area and tap density, enhancing battery performance with superior rate capability and initial capacity. However, this morphological optimization induces severe interfacial side reactions, causing rapid capacity fading. Herein, this study reports a novel wet chemistry coating method using hydrogen peroxide as an activation agent. Inspired by niobium-based oxide coatings for lithium-ion battery materials, this method is adapted for the sodium system with P2-type $Na_{7/9}Mn_{6/9}Cu_{2/9}Fe_{1/9}O_2$ layered sodium oxides. Despite the adverse effect of hydrogen peroxide on active material performance, this coating method retains significant advantages in time efficiency and scalability with uniform coating on the active material surface. Consequently, the surface modified material achieves remarkable capacity retention of 97% after 200 cycles at a current rate of 120 mA g^{-1} within a voltage window of 1.5–4.2 V with presodiated hard carbon electrode, much higher than that of pristine material (54%). Postmortem analysis of cycled electrodes and electrochemical impedance spectroscopy results confirm the well-covered material surface with suppressed side reactions, extending the battery cycling life. Additionally, powder X-ray diffraction and X-ray photoelectron spectroscopy analyses validate the temperature-dependent coating and substitution behaviors of the coating material.

1. Introduction

Sodium-ion batteries (SIBs) have recently garnered significant interests as an alternative technology to lithium-ion batteries (LIBs) in the large-scale stationary storage and cheap electrical vehicle market,[1] driven by the uniform global distribution of sodium resources and the cost-effectiveness of using aluminum rather than copper as the negative electrode current collector.[2–4] Among the explored positive electrode materials, layered sodium oxides (Na_xTMO_2, TM = Mn, Fe, Co, and Ni, etc.) stand out due to their high specific energy, high tap density, and simple synthesis procedure.[4–6] According to the surrounding sodium-ion environment and oxygen layer stacking orders,[7] they can be classified into two major groups, P2- and O3-type layered oxides, where P/O stands for prismatic/octahedral sites of sodium ions in the layered structure and the number denotes the repeating layers per unit cell. Manganese-based P2-type materials have been extensively studied since the first report from Fouassier et al.[8] in the 1970s, owing to the high sustainability and cost effectiveness. Recently, Li et al.[9] reported the synthesis of P2-$Na_{7/9}Mn_{6/9}Cu_{2/9}Fe_{1/9}O_2$ (P2-NMCFO) via a conventional solid-state method. This material exhibits superior cycling performance and remarkable structural stability against air and water, with copper substitution eliminating the need of critical element for the nickel, while maintaining electrochemical activity. Nevertheless, the suboptimal rate capability is likely due to the particle inhomogeneity inherent to the solid-state synthesis, as the major drawback compared to other synthesis methods.[10,11] Our prior works have demonstrated that spray drying can enhance the material performance by tailoring the sinter activity to form nanoporous, hierarchically structured particles with high specific surface area.[12,13] Nevertheless, this morphological optimization also induces more serious interfacial side reactions between the electrolyte and the active material during battery cycling, resulting in rapid capacity fading. To mitigate this issue, more efforts on surface engineering are imperative.

From the various techniques employed for the coating of battery materials, the wet chemistry method is widely adopted with advantages in high homogeneity and less equipment

R. Xu, V. Mereacre, V. Trouillet, H. Geßwein, A. Benayad, D. Mikhailova, H. Ehrenberg, J. R. Binder
Institute for Applied Materials—Energy Storage Systems
Karlsruhe Institute of Technology
76344 Eggenstein-Leopoldshafen, Germany
E-mail: ruochen.xu@kit.edu
joachim.binder@kit.edu

R. Leiter, S. Fleischmann
Helmholtz Institute Ulm (HIU)
89081 Ulm, Germany

R. Leiter, S. Fleischmann
Karlsruhe Institute of Technology (KIT)
76021 Karlsruhe, Germany

Supporting information for this article is available on the WWW under https://doi.org/10.1002/batt.202500672

dependency.[14–17] Regarding the choice of proper coating agents, sufficient chemical/electrochemical stability and high electrical conductivity should be taken into account as concluded by Nunes et al.[18] Recent studies have highlighted niobium-based oxides (e.g., Nb_2O_5, $LiNbO_3$, and $NaNbO_3$) as promising coating candidates for both layered lithium/sodium oxides, owing to their ideal combination of the aforementioned properties.[19–21] Notably, Nb^{5+} possesses a comparable ionic radius to other transition metal (TM) ions (e.g., Ni^{2+}, Ni^{3+}, Cu^{2+}, and Mn^{3+}).[18] This similarity enables niobium-based oxides not only to form uniform coatings but also to partially substitute other TM ions after calcination at high temperature (>600 °C).[20,22] Moreover, the strong Nb—O bonding resulting from the high oxygen affinity of niobium further enhances the structural stability of coated active material.[23,24] Although several studies have reported similar compositions, most of them provide only limited mechanistic insights, particularly regarding the temperature-driven substitution behavior of niobium. Furthermore, the uniformity of the surface coating is known to critically influence the resulting material performance.

Herein, we demonstrate a surface coating approach for the P2-NMCFO-positive electrode material using sodium niobium-based oxides via a novel wet chemistry method with hydrogen peroxide (H_2O_2) as an activation agent. This method has been intensively studied and optimized in our group for lithium-positive electrode materials such as $LiNi_{0.6}Mn_{0.2}Co_{0.2}O_2$ (NMC-622)[25] and $LiNi_{0.5}Mn_{1.5}O_4$ (LNMO) spinel.[15] Specifically, the activation by H_2O_2 enhances the surface reactivity of the active material, which significantly reduces the reaction time while maintaining the uniformity of the coating layer. Electrochemical tests reveal that the surface-coated NMCFO achieves 97% capacity retention after 200 cycles at 120 mA g^{-1} when paired with a presodiated hard carbon electrode. This represents a marked improvement over the pristine material, which retains only 54% of its initial capacity under the same conditions. Energy-dispersive X-ray spectroscopy (EDX) line scans and transmission electron microscopy (TEM) were performed to characterize the coating uniformity. Furthermore, powder X-ray diffraction (PXRD) and X-ray photoelectron spectroscopy analyses confirm the temperature-dependent coating/substitution behaviors of niobium oxides as expected, giving more mechanistic insights into how to achieve a longer cycling life for active materials.

2. Results and Discussion

ICP-OES measurements were performed to determine the chemical composition of the as-synthesized materials, including the pristine (NMCFO), activated (H-NMCFO), and coated (Nb-NMCFO) samples with coating concentrations of 2.5, 5, and 10 wt.% (see Table S1, Supporting Information). Here, the term "activated" refers to the material treated only with the hydrogen peroxide. The designation "80" indicates that the powders were only dried in an oven at 80 °C without subsequent calcination. As a result, the pristine material agreed well with the target composition. Notably, both activated and coated materials exhibited significant sodium loss, attributable to the strong alkalinity of the active material in aqueous solution, reacting with acidic hydrogen peroxide and nitric acid. Moreover, the niobium content in the coated material did not increase correlatively with the applied volume of coating solution, suggesting a critical coating threshold of around 5 wt.%. Beyond this value, the excess of niobium salts may only precipitate as impurities and was subsequently removed during washing. Besides, we used a relatively high nominal niobium content of 5 wt.% instead of conventional lower values (e.g., 0.5 wt.%) in this study. This adjustment accounts for the inverse relationship between coating thickness and coating agent density as well as the substrate surface area, as found in our previous research.[15,26] Considering the specific surface area of our active material is tenfold higher than that of the LNMO active material (3.6 m^2 g^{-1} vs. 0.4 m^2 g^{-1}), the higher niobium content was necessary to ensure the formation of a nanoscale layer on the particle surface.

Figure 1a illustrates the typical surface coating procedure on the active material, while detailed experimental parameters are provided in the *Experimental Section*. The SEM images of corresponding materials are shown in Figure 1b–d and Figure S1, Supporting Information. Specifically, Figure S1, Supporting Information, shows the pristine and as-treated H-/Nb-NMCFO materials without subsequent calcination, along with magnified views of the particle surface. As described in the *Experimental Section*, all materials exhibited porous, spherical morphology, resulting from the spray-drying process. Notably, H-NMCFO-80 °C displayed a smoother surface compared to that of pristine material. Considering the sodium loss observed in the ICP-OES analysis (Table S1, Supporting Information) and the reduced CO_3^{2-} peak intensity in the subsequent XPS section, this could be attributed to a reaction between the hydrogen peroxide and the active material as well as the residual Na_2CO_3 from the synthesis. Regarding the surface of coated material, the observed salt residues were derived from the reactant mixture and subsequently crystallized during the calcination process at higher temperatures. Despite the relatively small quantity of the coating component (considering the high specific surface area of the active material), thin and well-distributed surface layers were observed for calcined niobium-coated materials, as shown in Figure 1b,d. For better comparison, the particle surface of both H-NMCFO materials calcined at the same temperatures is also presented in Figure 1c,e. While the transition of niobium coating layer from amorphous to crystalline has been previously reported in lithium-based system,[20] our analysis reveals no distinct crystalline features on the surface of the coated materials calcined at 750 °C compared to the hydrogen peroxide control experiment. However, localized crystalline areas are observed at particle edges, as indicated by the arrow in Figure 1d, suggesting a facet-dependent reactivity similar to that reported in Li-NMC systems.[27] According to DFT calculations, the (012) surfaces exhibit higher reactivity than the (104) surfaces due to oxygen vacancy formation, making oxygen removal easier in that case.[27] Although the specific reactive facets in our P2-type material remain unclear, such anisotropic surface behavior is consistent with our results on surface reactivity variations. Moreover, complementary EDX mapping of Na, Mn, Cu, Fe, and Nb reveals

Research Article
doi.org/10.1002/batt.202500672
Chemistry Europe
European Chemical Societies Publishing

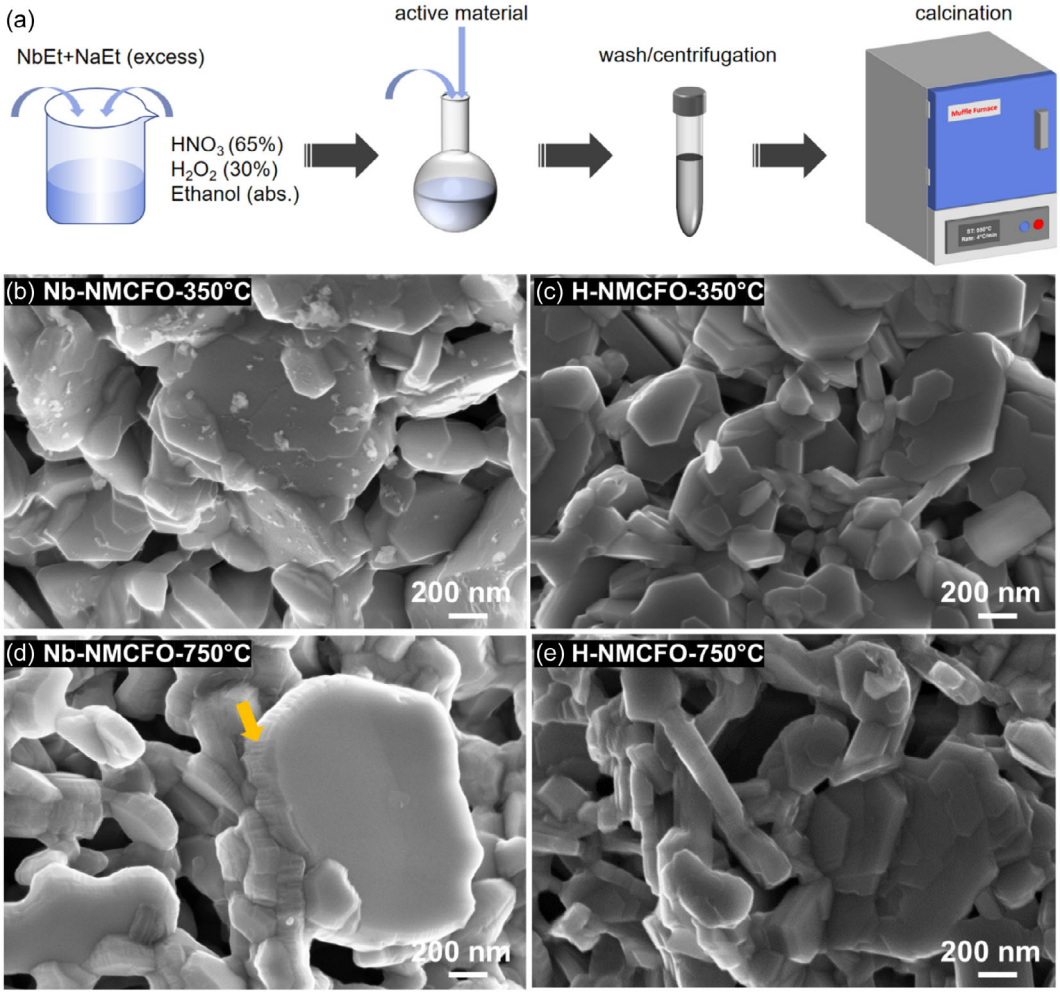

Figure 1. a) Schematic illustration of the surface coating fabrication on active materials via wet chemistry approach. SEM images of Nb-NMCFO and H-NMCFO calcined at b,c) 350 °C and d,e) 750 °C. The arrow indicates the local crystallinity at active material edge surface.

copper agglomeration in discrete regions (Figure S3, Supporting Information), indicating potential crystal structure changes and were subsequently identified as copper oxide phases, with further details provided in the PXRD section. Additionally, in order to further investigate the effect of surface coating toward the material surface area, the specific surface area of the active materials was measured and calculated with the BET method for the coated and the temperature-treated materials calcined at various temperatures (Figure S2b, Supporting Information). The results indicate that the $NaNbO_3$ coating slightly increases the surface area compared with the pristine material, since the coating is not smooth, but also porous. Meanwhile, no noticeable change in porosity was observed in the SEM images. At lower calcination temperatures (<450 °C), the temperature effect itself has little influence on surface area or morphology. However, at higher temperatures (>750 °C), particle sintering becomes evident, leading to a more compact structure, as observed in both NMCFO-750 °C and Nb-NMCFO-750 °C.

The PXRD patterns of 5 wt.% Nb-NMCFO after calcination at various temperatures are shown in **Figure 2**a, along with the lattice parameter changes as a function of the calcination temperature. To understand the effects of temperature and hydrogen peroxide treatment on the crystal structure of the active material (Figure 2b), data from the untreated reference NMCFO material are also included for comparison. As mentioned above, at calcination temperatures above 650 °C, additional reflections are observed for Nb-NMCFO and identified as $NaNbO_3$ (S.G. *Cmcm*, PDF-01-083-5090), indicating temperature-dependent crystallization in the coating layer. Moreover, when the calcination temperature was increased from 650 to 750 °C, the amount of $NaNbO_3$ slightly decreases from 3.76 (±0.22) wt.% to 3.45 (±0.16) wt.%, accompanied by an increase in the amount of CuO (S.G. *C2/c*, PDF-01-073-6023). This may suggest a temperature-driven substitution behavior of niobium, where copper migrated from the bulk to the surface and formed copper oxide deposits. The observed copper oxide segregation is attributed to the relatively low solubility of Cu^{2+} compared to other transition metals in TM-O layers, consistent with prior doping studies in Cu-based layered sodium oxides.[28] Further evidence is provided by changes in the lattice parameters, where both the H-NMCFO and Nb-NMCFO series

Research Article
doi.org/10.1002/batt.202500672
Chemistry Europe
European Chemical Societies Publishing

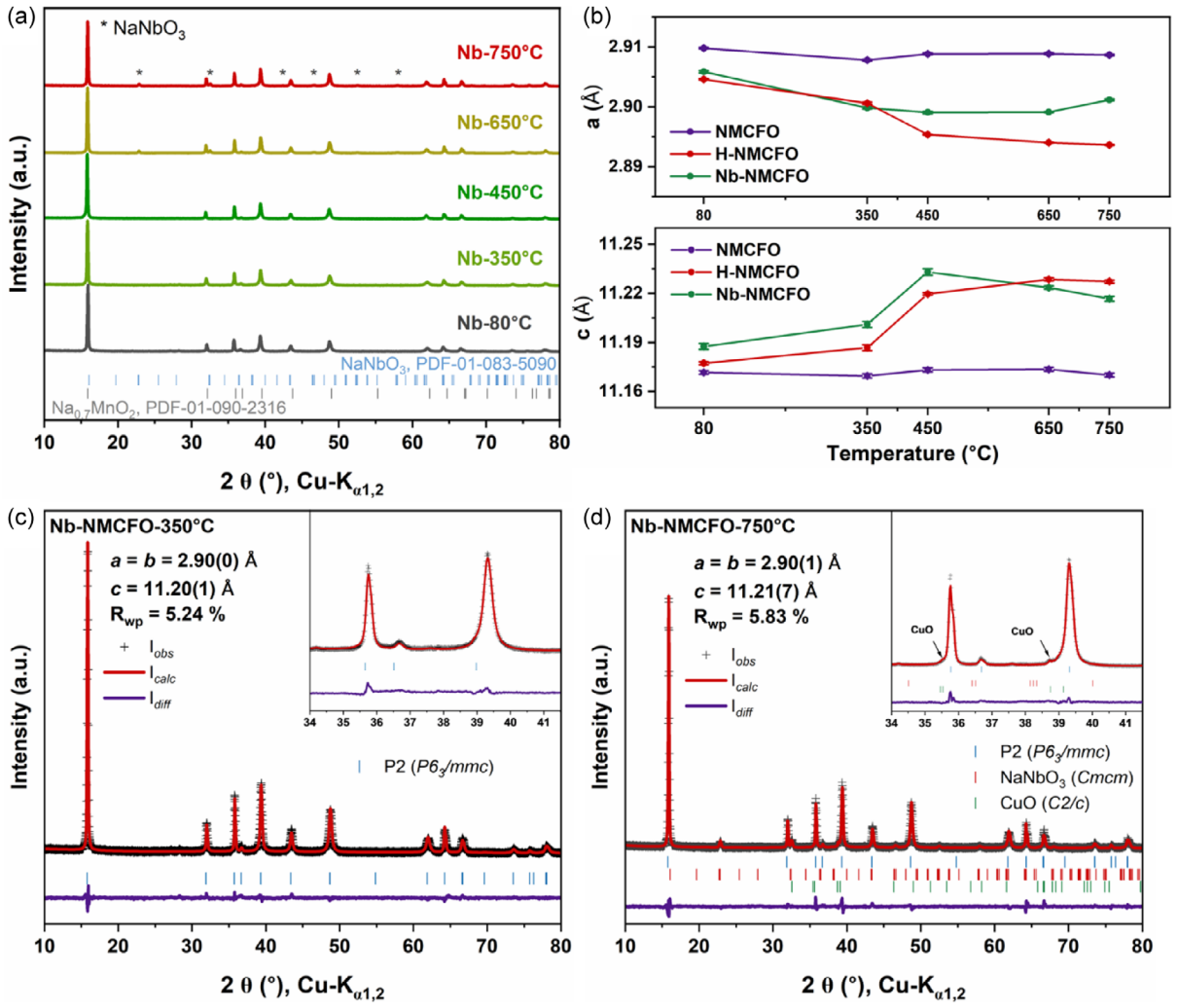

Figure 2. a) PXRD patterns of 5 wt.% Nb-NMCFO after calcination at various temperatures. b) Lattice parameter changes of NMCFO, Nb-NMCFO, and H-NMCFO after calcination (error bars reflect uncertainties from Rietveld refinements multiplied by the Berar-factor).[38] Rietveld refinement results of Nb-NMCFO calcined at c) 350 °C and d) 750 °C with enlarged regions of the XRD patterns 34° and 41.5°.

exhibit similar trends at low calcination temperature (450 °C), including a decrease in the initial lattice parameter *a* and an increase in *c*. These changes are likely related to the treatment with hydrogen peroxide that leads to oxidation of the active material and Na-leaching from the structure. This is evident from the comparison of *a* lattice parameter, which is directly proportional to the TM-O distance. It is smaller for the H-NMCFO and Nb-NMCFO materials compared to the pristine sample. This suggests oxidation of transition metals in the structure due to the charge compensation. Additionally, instead of Na, some H_2O molecules may be incorporated into the structure during H_2O_2 treatment. Upon heating, these H_2O molecules are removed, which could explain the more pronounced changes in the unit cell parameters compared to the initial material. When the calcination temperature exceeded 450 °C, Nb-NMCFO exhibited an increase in lattice parameter *a* and a decrease in *c*. The decrease in *c* could be related to the gradual incorporation of niobium and the extraction of copper ions, considering the larger ionic radius of Cu^{2+} (0.73 Å) compared to that of Nb^{5+} (0.64 Å).[18] Along the *a*-direction, a conventional positive thermal expansion of the crystal structure was observed. In contrast, the crystal structure of the untreated active material is less affected by temperature variations, as evidenced by the nearly constant lattice parameters across all calcination temperatures. The lattice parameters, Na ion occupancies, percentages of minor phases, and R_{wp} values for NMCFO, Nb-NMCFO, and H-NMCFO calcined at various temperatures were obtained by Rietveld refinement and summarized in Table S2, Supporting Information. It is worth noting here that the Na occupancies were refined by fixing the total Na content based on ICP-OES results, with Na_e refined independently and Na_f calculated by subtracting the Na_e content from the total Na content. The corresponding refined PXRD patterns for NMCFO, H-NMCFO, and Nb-NMCFO series calcined at 350 and 750 °C are presented in Figure S4, Supporting Information, and Figure 2c,d.

The diffraction patterns of all materials are nearly consistent with the corresponding P2 phase, confirming that the crystal

Research Article
doi.org/10.1002/batt.202500672
Chemistry Europe
European Chemical Societies Publishing

structure of the active material remained intact after the hydrogen peroxide treatment and coating procedure. An in-plane Na^+/vacancy ordering would be reflected by characteristic peaks at 27.1° and 28.2°, which are sometimes observed in the diffraction patterns with weak intensities. To better understand this ordering, the corresponding Na_e and Na_f site occupancies in the prismatic structure were obtained from the refinements, where Na_e and Na_f refer to the edge-shared and face-shared Na sites with adjacent MO_6 octahedra, respectively.[29] The Na_e occupancy is very close in all three samples prior to the thermal treatments, whereas the Na_f occupancy decreases consequently from the untreated material to activated and to coated one. Increasing the temperature only slightly reduces the Na_f occupancy and increases Na_e occupancy for all samples, consistent with Pauling's theory that Na_e site is energetically more favorable.[30] At the same time, rising temperature leads to complete vanishing of ordering-related (superstructure) reflections in case of the H- and Nb-NMCFO samples, as shown in Figure S4, Supporting Information, for 750 °C. In contrast, these reflections remain present in the NMCFO-750 °C sample, pointing to a kinetic or thermodynamic barrier for a random sodium distribution between the TM-oxygen layers, what should be studied in a future work.

To gain further insights into the surface environment changes, XPS spectra of C 1s, Cu $2p_{3/2}$, and Nb 3d are provided in **Figure 3**. The C 1s spectra revealed a significant reduction in CO_3^{2-} concentration (289.4 eV) on the particle surface in both H-/Nb-NMCFO-350 °C, confirming the reaction between acidic hydrogen peroxide and residual carbonates from synthesis. For manganese oxidation analysis, instead of plotting the individual Mn 3s regions, the energy gap (ΔE) between both peaks of the multiplet splitting of Mn 3s peaks was calculated for all materials (Figure 3b) to enable an evaluation of the oxidation state. As an example, the XPS spectrum for the Mn 3s region of the pristine material is shown in Figure S5a, Supporting Information. For more information, the Mn 2p region of pristine and Nb-NMCFO-350 °C is also included in Figure 5b. According to the early research,[31] ΔE is inversely proportional to the mean oxidation state of manganese with established reference values of 5.5 eV (Mn^{2+}), 5.0 eV (Mn^{3+}), and 4.5 eV (Mn^{4+}). Our data show a gradual decrease in ΔE from the pristine material to Nb-NMCFO-350 °C. This indicates that Mn is oxidized after calcination, likely to compensate for the charge imbalance caused by sodium loss during hydrogen peroxide activation and the subsequent coating process, given that Cu^{2+} and Fe^{3+} are the most stable oxidation states of Cu

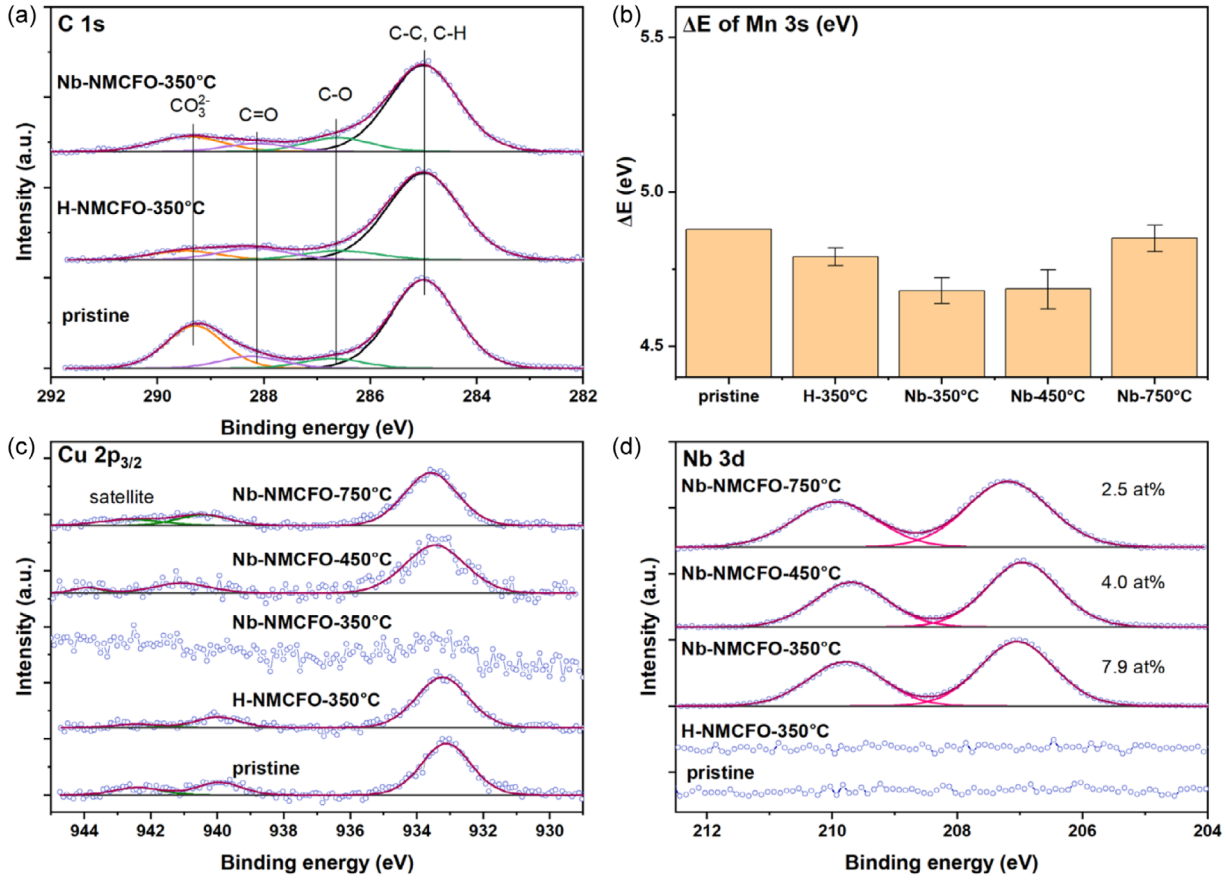

Figure 3. XPS spectra of a) C 1s, c) Cu $2p_{3/2}$, and d) Nb 3d. b) To minimize ambiguity, Mn 3s spectra for all samples are not presented here but as the energy gap (ΔE) between both peaks of the multiplet splitting of Mn 3s are shown. All spectra were normalized to the maximum of intensity and the niobium concentrations are presented in atomic percent (at.%).

Research Article
doi.org/10.1002/batt.202500672
Chemistry Europe
European Chemical Societies Publishing

and Fe under ambient conditions, respectively. Furthermore, the ΔE value for the Nb-NMCFO series remained nearly unchanged below 450 °C but reversed at 750 °C, indicating the reduction of manganese. Figure 3c,d demonstrates the low copper and high niobium concentrations in Nb-NMCFO-350 °C compared to other samples, further supporting the uniform coverage of the particle surface by the niobium coating at this temperature. It is noted that all spectra here are normalized to the maximum intensity and the niobium concentrations are presented in atomic percent. The characteristic doublet at 207–209 eV conclusively verified the +5 oxidation state of niobium.[19] The temperature-dependent decrease in surface niobium concentration might be attributed to the growth of $NaNbO_3$ crystallites which would no longer cover the surface of the active material or to the migration of niobium from the surface into the bulk structure at elevated temperatures. This is further supported by the observed reduction of manganese, which results from charge balance considerations, given the high oxidation state of Nb^{5+} compared to $Mn^{3+/4+}$. Considering that XPS measurements provide only averaged information, advanced analyses were further conducted to track the temperature-induced transformations.

To investigate the morphology of the niobium salt and its distribution on the active material, SEM and TEM analyses were performed. First, a Nb-NMCFO-350 °C electrode was prepared with smooth surface by ion etching as shown in Figure S6, Supporting Information. The particle exhibited high porosity as expected, and compared to other elements (Na, Mn, Cu, and Fe), the niobium signals appeared to be concentrated on the secondary particle surface. However, these locally rich regions are the accumulated Na salts and cannot be correlated with the thickness of coating layer. More interesting are the pore regions within the secondary particle, where the electrolyte penetration and the electrode–electrolyte interfacial reactions can occur. With this aim, an EDX line scan was performed across a secondary particle (**Figure 4**a), with the corresponding elemental distribution spectrum shown in Figure S7, Supporting Information. This line scan reveals an increased niobium signal relative to the Na/Mn signals at the pore space of the secondary particles, which confirms the penetration of the spray-dried powder particles with the Nb-containing solution during the wet chemical coating process and the formation of a surface coating layer. The reduced Na/Mn signals indicate the presence of pore spaces lacking bulk material, while the sharp rise in niobium signals suggests niobium coverage of primary particles and the nanoscale thickness of the coating layer. Residual Na/Mn signals in pore areas may result from either tightly packed underlying particles below the detection limit or signal integration from nearby particles, as the line scan thickness is non-negligible.

Therefore, TEM analysis was performed on Nb-NMCFO-350 °C to more precisely investigate the uniformity of the niobium coating layer. However, due to the larger particle size, the analysis was performed only on powder material without further sectioning. As shown in the bright–field and HAADF–STEM images (Figure 4c,e), the secondary particle consists of densely packed primary particles, making it challenging to distinguish between the active material and the coating layer as shown in the HRTEM image in Figure 4d. Nonetheless, STEM-EDX mapping confirmed the presence of a distinct layer with niobium signals, verifying the existence of the coating layer on the primary particles. Meanwhile, TEM analysis was also performed on Nb-NMCFO-750 °C. As shown at spot 1 (Figure S8, Supporting Information), niobium displays a rather inhomogeneous distribution compared to other elements,

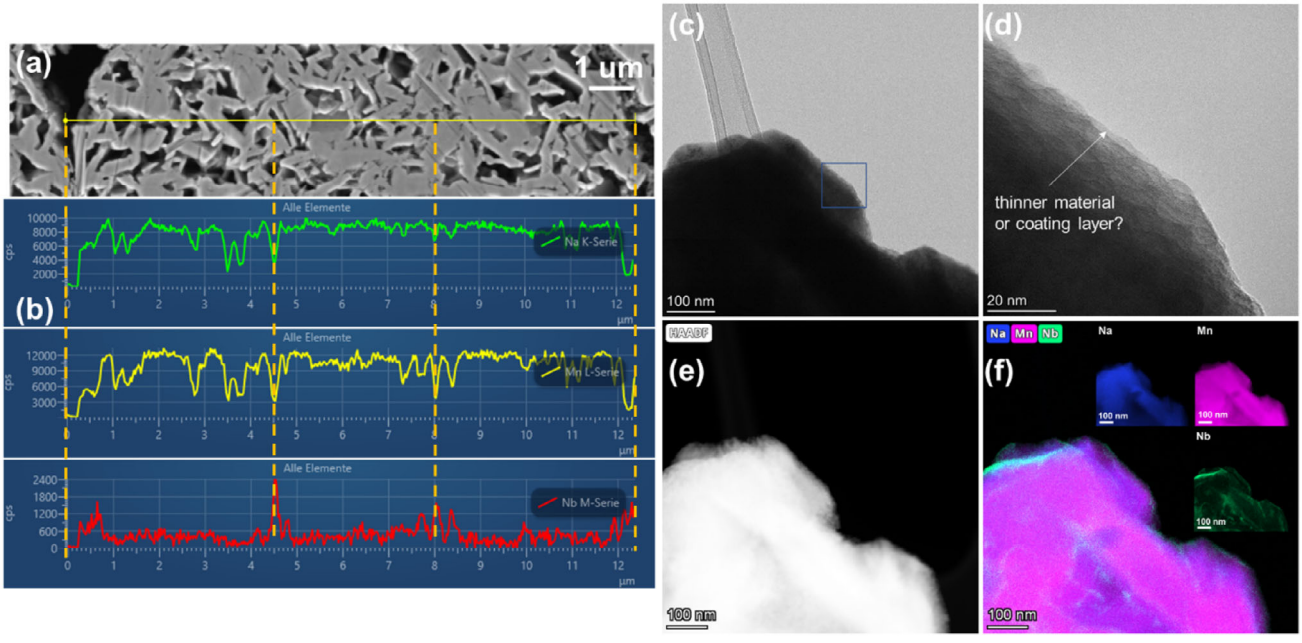

Figure 4. a) Cross-sectional electrode SEM image of the Nb-NMCFO-350 °C and b) EDX line scan profiles of Na, Mn, and Nb. TEM images of c) bright-field overview, d) high-resolution TEM (HRTEM), e) high-angle annular dark-field scanning TEM (HAADF–STEM), and f) STEM-EDX elemental mappings of Na, Mn, and Nb.

Research Article
doi.org/10.1002/batt.202500672
Chemistry Europe
European Chemical Societies Publishing

performing an "island-like" growth of $NaNbO_3$ crystallites at this temperature. To further analyze the crystallinity, Fast Fourier Transform (FFT) analysis was performed on the marked "Nb-rich" area (#2). The results showed only weak crystalline spots with an amorphous outer surface, which might be attributed to partially crystalline $NaNbO_3$ or the formation of Na_2CO_3 on the surface, as the active material dominates in this region. To gain further insight, spot 2 (Figure S9, Supporting Information) from another particle was examined, where the Nb signal was much stronger than that of Mn, indicating a higher concentration of $NaNbO_3$ compared to the active material. In this case, the FFT analysis of the marked area revealed lattice spots at 2.2 nm^{-1}, corresponding to a d-spacing of 4.5 Å, which matches well with the (111) plane of $NaNbO_3$.

The electrochemical performance of the niobium coated materials is presented in **Figure 5** and Figure S10, Supporting Information, along with the results of the reference materials (solely temperature and hydrogen peroxide treatment). Figure 5a shows the charge–discharge profile of the formation cycle for the pristine, temperature-treated, hydrogen peroxide-treated, and niobium-coated materials calcined at 350 °C to understand the effects of these factors on battery performance. As expected, the NMCFO-350 °C exhibited a profile similar to that of the pristine material, indicating that the temperature solely does not significantly affect the material performance. However, both H-/Nb-NMCFO-350 °C showed a significant decrease in the initial desodiation capacities, with values of 82 and 78 mAh g^{-1}, respectively, compared to the pristine material (104 mAh g^{-1}). This reduction in capacity is attributed to the acidic treatment during the coating process, which partially consumed the sodium inventory. Nevertheless, these two materials exhibited more plateau like behaviors, likely due to the sodium reordering within the crystal structure during cycling. Long cycling stability tests (Figure 5b) were conducted within the same voltage range at 1C (1C = 100 mA g^{-1}), and for better comparison, the capacities at the 20th and 120th cycles were used to calculate capacity retention. As a result, the pristine material delivered a higher initial capacity of 97 mAh g^{-1} at this current rate but remained only 82% of its initial capacity after 120 cycles. In contrast, the T-/H-NMCFO-350 °C materials showed similar initial capacities but slightly better retention of 86 and 84% after 120 cycles, respectively. This improvement may be related to the increased crystallinity of the active material owing to the additional thermal treatment. Notably, Nb-NMCFO-350 °C achieved the best capacity retention with 95%, despite exhibiting the lowest capacity (90 mAh g^{-1}). By comparing other factors such as temperature and hydrogen peroxide, this superior performance is attributed to the uniform niobium coating on the material

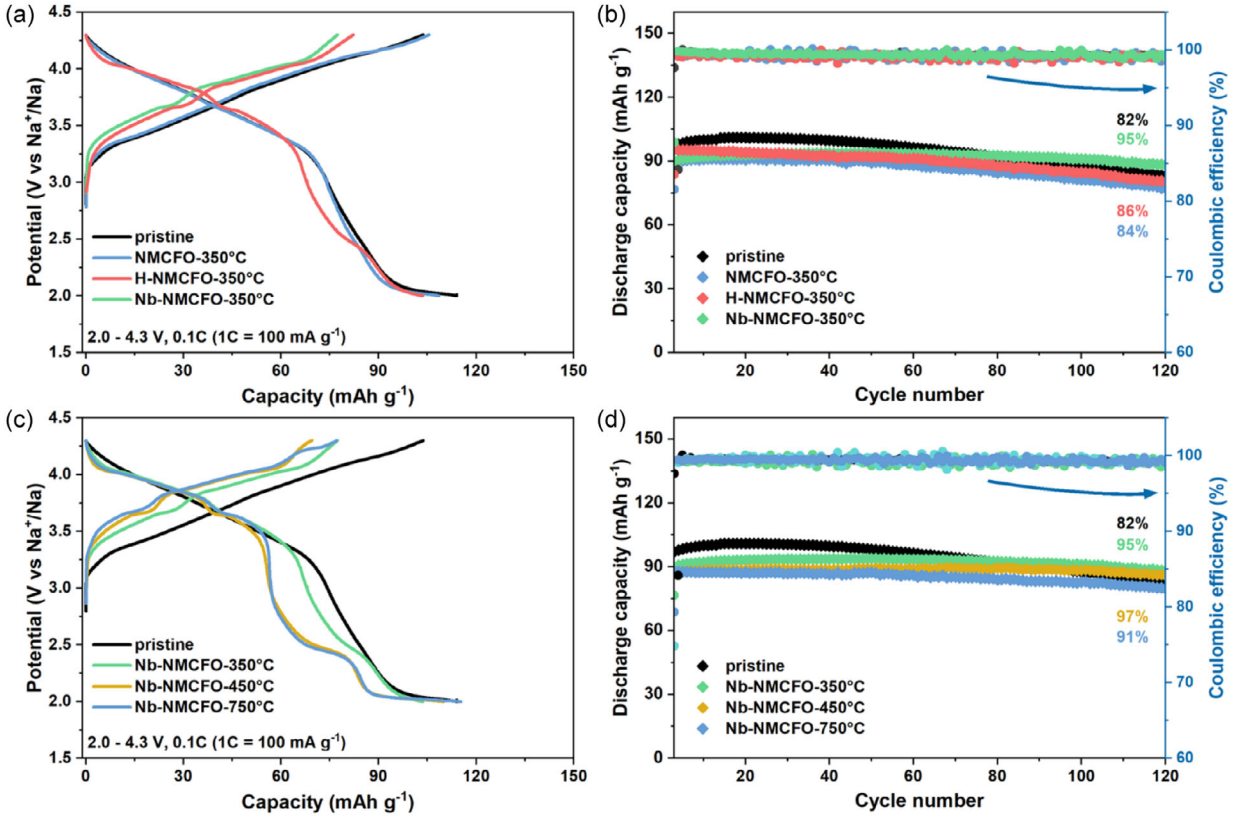

Figure 5. a) Charge-discharge profiles of the pristine and T-/H-/Nb-NMCFO-350 °C materials at 0.1C. b) Cycling stability tests of the materials at 1C for 120 cycles. c) Charge-discharge profiles of the pristine and Nb-NMCFO materials calcined at 350, 450, and 750 °C measured at 0.1C. d) Cycling stability tests of the materials at 1C for 120 cycles. All battery tests were performed within a voltage range of 2.0–4.3 V and 1C corresponds to 100 mA g^{-1}. Electrolyte: 1 M $NaPF_6$ in EC/PC (1:1, wt.%) with 5 wt.% FEC.

surface, inhibiting interfacial reactions and enhancing structural stability. To further investigate the impact of the surface coating on the active material, the charge–discharge profiles and corresponding $\frac{dQ}{dV}$ curves of the pristine and Nb-NMCFO-350 °C materials were analyzed for the 1st, 50th, and 100th cycles at 1C (Figure S10 a–d, Supporting Information). Both materials exhibited differences between the first and subsequent cycles, likely due to the activation process that explains the initial capacity increase during early cycles. Moreover, the niobium-coated material displayed well-overlapped profiles, indicating stable structure during battery cycling. In contrast, the pristine material showed a decrease in capacity and redox peak intensities, suggesting significant structural degradation over time. The electrochemical performance in terms of capacities for all materials are summarized in Table S3, Supporting Information.

The effect of the additional thermal treatment of the coated active materials is shown in Figure 5c,d. Up to 450 °C, a decrease in initial desodiation capacities was observed. However, increasing the calcination temperature to 750 °C led to an increase of the reversible desodiation capacity up to 77 mAh g^{-1}. This might be due to the crystallization of residual, amorphous sodium-containing phases that could act as an additional sodium source. Additionally, more distinct plateaus at 2.5 and 3.5 V emerged for materials calcined at 450 and 750 °C, which may be attributed to the Mn^{3+}/Mn^{4+} redox couple and sodium vacancy ordering rearrangement.[32,33] All three niobium-coated materials exhibited better capacity retention than the pristine material, despite lower initial capacities at the high current rate. This may result from the lower conductivity of the coating layer compared to the active material. The influence of the niobium concentration is shown in Figure S10e,f, Supporting Information, and as a result, initial desodiation capacity decreased as niobium concentration increased from 2 to 10 wt.%. This is related to the increasing amount of hydrogen peroxide in the coating solution and sodium consumption. The 5 wt.% variant demonstrated optimal cycling stability, while the 10 wt.% variant showed no further improvement, likely due to niobium saturation, as evidenced by the ICP-OES results.

Additionally, in order to investigate the investigate beneficial effect of $NaNbO_3$ coating toward the Na diffusion, the apparent diffusion coefficients were calculated from the CV data and the corresponding results have been included in Table S5, Supporting Information. As a result, the coated samples calcined at various temperatures consistently show higher apparent diffusion coefficients at the anodic/cathodic peaks at ≈4.1/3.9 V compared with the pristine material. According to Li et al.[9] these peaks are associated with the Cu^{2+}/Cu^{3+} redox couple. The enhanced diffusion coefficients observed for the coated samples indicate that the $NaNbO_3$ surface layer facilitates Na^+ transportation in this region. In addition, the coated materials exhibit improved capacitive response as shown in Figure S11, Supporting Information, in agreement with the findings of Lavela et al.[21] These results suggest that the $NaNbO_3$ coating contributes to improved interfacial Na^+ transportation during cycling. However, it is worth mentioning that the coated materials deliver notable lower capacities at high current rates compared with the pristine material, likely due to its intrinsically lower electronic conductivity. Therefore, while the coating enhances interfacial Na^+ diffusion, it does not necessarily translate into improved rate capability at high C-rates. Details of the calculation are provided in the Supporting Information.

Owing to the superior performance in a sodium half-cell, 5 wt.% Nb-NMCFO-350 °C was selected for the full-cell testing with presodiated hard carbon, employing an enlarged voltage range of 1.5–4.2 V. The presodiation followed the previously described protocol in electrochemical measurement and its charge–discharge profile is shown in Figure S12a, Supporting Information. Full-cell testing comprised two formation cycles at 12 mA g^{-1} (0.1C) followed by 200 cycles at 120 mA g^{-1} (1C). As shown in **Figure 6**a,b, although Nb-NMCFO-350 °C exhibited lower initial capacities (≈73 mAh g^{-1} for the initial charge capacity and 101 mAh g^{-1} at 1C, based on the positive electrode mass), it demonstrated outstanding cycling stability with 97% capacity retention after 200 cycles. In contrast, the pristine material delivered 123 mAh g^{-1} at the 10th cycle (1C) but retained only 80 and 54% capacity after 100 and 190 cycles, respectively. Notably, even when excluding the activation period, the coated material maintained superior stability with 92% capacity retention between the 100th and 200th cycles.

Electrochemical impedance spectroscopy (EIS) measurements were performed on full cells in their fully charged state (4.2 V) at selected cycles to monitor the interfacial impedance evolution. The corresponding Nyquist plots are shown in Figure 6c,d. It should be noted that the "first cycle" measurement was performed after two formation cycles and prior to the long cycling stability tests. To determine the most appropriate equivalent circuit model, distribution of relaxation time (DRT) analysis was performed on the EIS data, complemented by the frequency dependent analysis of Nyquist plots. Figure 6e,f reveals five distinct peaks in the frequency range of 100 kHz to 10 mHz on both materials, corresponding to five different time constants. The corresponding frequency-dependent analysis of the Nyquist impedance spectra is shown in Figure S12b,c, Supporting Information. While full-cell data alone provide limited information for precise DRT peak assignment, the comprehensive $LiCoO_2$ // graphite cell studies by Chen et al.[34] was drawn upon for guidance. Their work suggests that these peaks represent (P1+P2) surface film resistance R_{SF} in the high/middle frequency region, (P3+P4) charge transfer resistance R_{ct} at low frequency region, and P5 as Warburg impedance at frequencies below 0.1 Hz. Accordingly, an equivalent circuit model was adopted, comprising four R-CPE elements and a Warburg component, as shown in Figure S12d, Supporting Information. It is worth noting that although sodium diffusion occurs in both electrodes, for simplified modeling with a focus on the impedance changes, a single Warburg element was applied in the frequency range from 0.1 to 10^5 Hz, while the less relevant low-frequency Warburg region was excluded to achieve better fitting. The fitted resistance values are summarized in Table S4, Supporting Information, and fitting quality was verified through phase angle plots (Figure S13, Supporting Information). However, due to the limited knowledge and the challenges in distinguishing the contributions from hard carbon and the selected positive electrode materials, the reported values of R_{SF} and R_{ct} include both components. The Nb-coated sample exhibited an

Research Article
doi.org/10.1002/batt.202500672
Chemistry Europe
European Chemical Societies Publishing

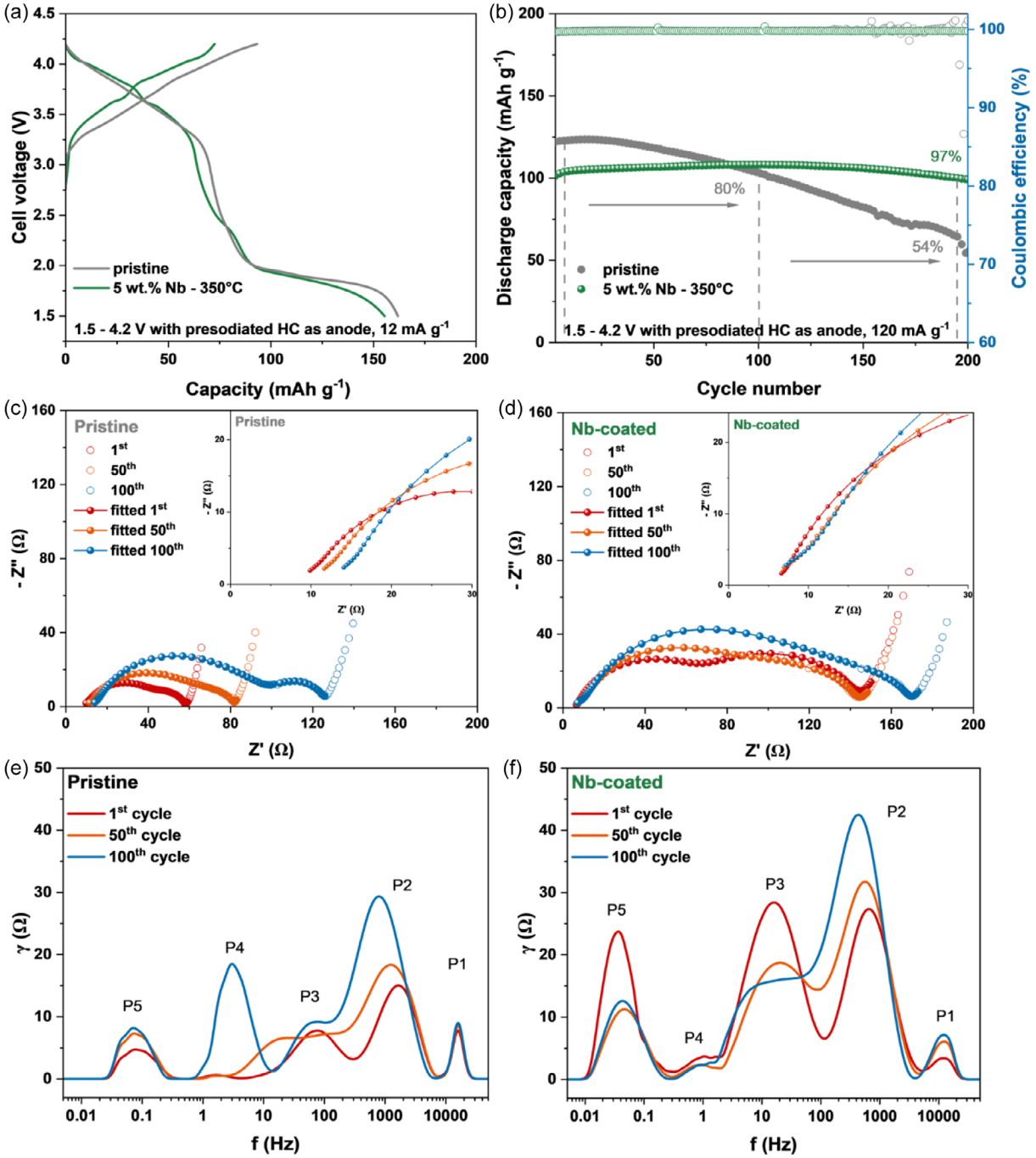

Figure 6. a) Charge–discharge profiles of the pristine and Nb-NMCFO-350 °C materials in full cell configuration using presodiated hard carbon electrodes, cycled between 1.5 and 4.2 V at a current rate of 12 mA g^{-1}. b) Cycling stability tests of the materials at 120 mA g^{-1} for 200 cycles. Nyquist plots of electrochemical impedance spectroscopy for c) pristine d) Nb-NMCFO-350 °C // HC full cells measured at the fully charged state (4.2 V) at different cycles, along with the corresponding distribution of relaxation time e,f) calculated from the EIS data.

initial R_{ct} of 73.5 Ω (14.7 + 58.8 Ω) after the formation cycles, which decreased to 56.4 Ω (20.6 + 35.8 Ω) after 100 cycles. The initially high resistance possibly reflects the less conductive coating layer, while the subsequent reduction suggests an activation process. In contrast, the cell with pristine material exhibited significant increases in both ohmic (from 8.8 to 12.5 Ω) and charge transfer resistances (from 17.1 Ω [16.1 + 1.1 Ω] to [15.4 + 27.0 Ω]) after 100 cycles. Since the hard carbon electrodes were from same electrode sheet and treated identically, the increased impedance can be attributed to the positive electrode, with the rise indicating continuous electrolyte decomposition and interfacial degradation in the pristine material. Furthermore, both materials exhibited increasing surface film resistances, consistence with continuous CEI/SEI formation. Overall, the mitigated impedance increase on the niobium-coated material indicates the enhanced interfacial stability and suppressed electrolyte decomposition.

Research Article
doi.org/10.1002/batt.202500672
Chemistry Europe
European Chemical Societies Publishing

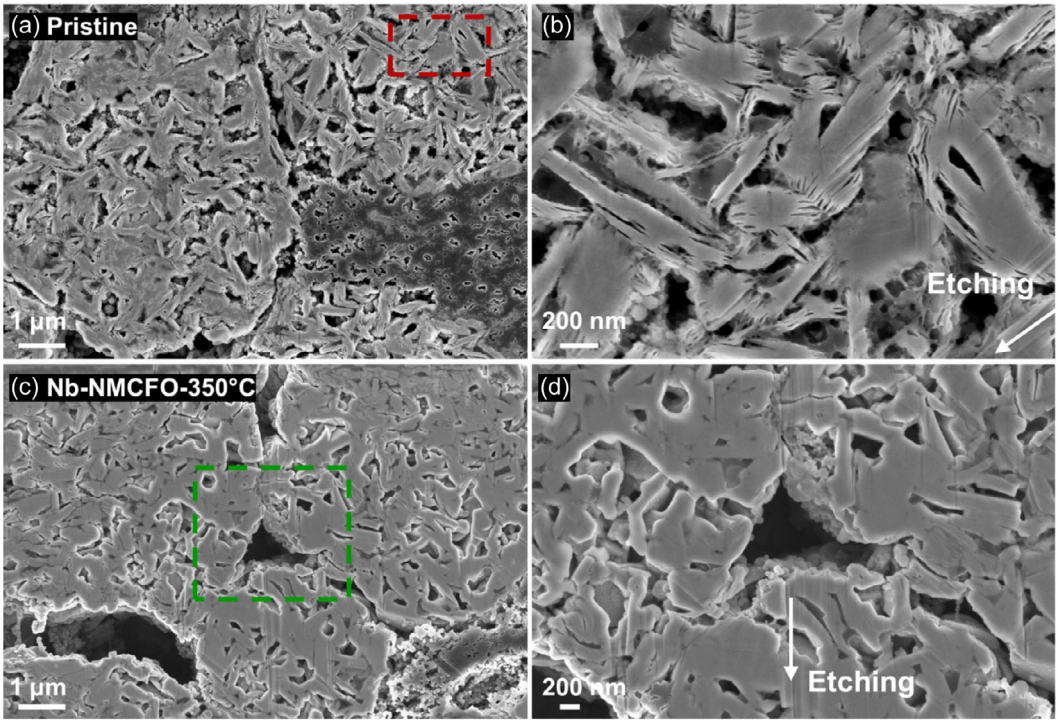

Figure 7. Postmortem SEM analysis of cycled electrodes: a) pristine and c) Nb-NMCFO-350 °C materials, with corresponding high magnification views shown in b) and d), respectively.

After 200 cycles, both full cells were disassembled in a glovebox. The corresponding positive and hard carbon electrodes were rinsed with DMC, dried, and prepared for postmortem analysis. XPS analysis of the cycled HC electrodes were carried out to access the transition metal dissolution from the positive electrode, which could be deposited on the negative electrode via electrolyte transport and hinder the sodium ion diffusion. As shown in Figure S14d, Supporting Information, while fluorine signals from electrolyte decomposition were detected on both hard carbon electrodes, signals from transition metals (Mn, Cu, Fe) were negligible. This suggests that the rapid capacity decay observed in the pristine material was not primarily caused by the transition metal dissolution. Moreover, the HC electrode paired with the coated positive electrode exhibited a noticeable feature in terms of F 1s spectra (Figure S14d, Supporting Information). According to the J. Fondard et al.[35] the peak at ≈686.5 eV corresponds to residual $NaPF_6$ salt on the electrode surface, whereas the peak at ≈684 eV is associated with NaF as the degradation product. The lower intensity of the NaF signal observed for the coated electrode after cycling highlights the protective effect of $NaNbO_3$ coating with suppressed surface degradation, thereby contributing to the enhanced interfacial and structural stability. Therefore, postmortem analysis of the cycled pristine and Nb-NMCFO-350 °C electrodes were conducted to investigate the particle structural degradation. As shown in **Figure 7**, the primary particles from the pristine electrode exhibited severe cracking, consistent with the increased interfacial resistance discussed earlier in EIS results. In contrast, particles from the Nb-NMCFO-350 °C electrode well maintained structural integrity, demonstrating the uniform niobium coating can effectively enhance interfacial stability and mitigate electrolyte decomposition.

3. Conclusion

In summary, this study demonstrates that a uniform $NaNbO_3$ surface coating can effectively protect the spray-dried active materials with high specific surface area. The coating simultaneously mitigates electrolyte decomposition and suppresses particle cracking during battery cycling, though inherent tradeoffs exist in sodium loss from hydrogen peroxide activation and reduced conductivity compared to lithium niobate analogs. The coated material achieves remarkable cycling stability (97% capacity retention after 200 cycles), representing a significant improvement from the pristine material with only 54% retention. Furthermore, the advantages of scalability, time-efficiency, and uniformity provided by this novel wet chemical method make it a practical strategy for extending sodium-ion battery cycle life. Future optimizations should focus on other positive electrode materials with higher sodium reserves and alternative coating compositions that balance high conductivity with protective functionality.

4. Experimental Section

Synthesis of Positive Electrode Material

A multistep synthesis process was conducted to produce the nanoporous, hierarchically structured P2- $Na_{7/9}Mn_{6/9}Cu_{2/9}Fe_{1/9}O_2$ (P2-NMCFO) positive electrode material. In contrast to the sol–gel method reported in our prior work,[12] a simple solid-state synthesis was adopted to obtain the pure phase active material as the first step of this work. Stoichiometric amounts of Na_2CO_3 (anhydrous, VWR Chemicals), Mn_2O_3 (98%, Thermo Scientific), CuO 98%,

Sigma–Aldrich), and Fe_2O_3 (99+%, Sigma–Aldrich) were mixed and ground in a Pulverisette 5 planetary mill (Fritsch) using 1.5 mm ZrO_2 milling balls (ball to powder ratio of 10:1 by mass) in isopropanol ($\geq$ 99.7%, VWR Chemicals, solvent to powder ratio of 2:1 by mass) at 447 rpm for 10 h. After removing the isopropanol, the dried precursor was calcined at 900 °C for 12 h in synthetic air with a ramp rate of 5 K min^{-1}. After cooling, the remaining powder was then ground again in the same ball milling jar with deionized water as dispersion agent to form an aqueous suspension of fine primary particles and prepared for spray drying. The resulting spray-dried powder (cyclone and tower fractions) was collected, sieved, and subsequently calcined again at 700 °C for 6 h in synthetic air. Consequently, the porous NMCFO material (after second calcination) exhibited a higher specific surface area of 3.6 m^2 g^{-1}, compared to the particles synthesized via the conventional solid-state method (after first calcination) with only 1.4 m^2 g^{-1}. For further details regarding the synthesis parameters and experimental setup, please refer to our prior work.[12]

Surface Coating Fabrication via a Wet Chemistry Approach

The sodium niobium-based oxide $NaNbO_x$ surface coating on the active material was fabricated via a wet chemistry approach. In a typical process, 0.301 g niobium(V) ethoxide ($Nb_2(OC_2H_5)_{10}$, 99.95% metals basis, Sigma–Aldrich) and 0.075 g sodium ethoxide (CH_3CH_2ONa, with 10% excess, 95%, Sigma–Aldrich) were dissolved in 20 and 40 mL absolute ethanol (HPLC grade, Supelco, Sigma–Aldrich), respectively. The solutions were then combined, followed by the addition of 20 mL of hydrogen peroxide (H_2O_2, 30%, Sigma–Aldrich), 40 mL deionized water, and 0.1 mL nitric acid (HNO_3, 65%, VWR Chemicals) to obtain a clear coating solution. The acid was introduced to get a clear solution and neutralize residual sodium carbonate on the active material surface. 1.2 g of NMCFO and 50 mL absolute ethanol were added into a round bottom flask. As reported in our prior work,[15] the reaction between hydrogen peroxide and active material surface is highly exothermic, accompanied by vigorous gas evolution. Therefore, 46.4 mL of the coating solution (containing $\approx$ 5 wt.% $NaNbO_x$) was added dropwise under continuous stirring. In this work, the reaction was not as violent as reported earlier but a significant increase of solution temperature (from 25 to $\approx$40 °C) was observed. The mixture was stirred until no obvious gas evolution was observed (typically within 30 min). To ensure complete decomposition of residual hydrogen peroxide, stirring was continued for additional 10 min. The suspension was then decanted and the powder was washed with deionized water, centrifuged, dried, and calcined in air firstly at 250 °C for 2 h and at target temperatures for 5 h with heating rate of 4 K min^{-1}. After cooling down to room temperature with a cooling rate of 2 K min^{-1}, the coated material was transferred into a glovebox for later use. The obtained materials were labeled as Nb-NMCFO-X °C. Considering the acidic nature of hydrogen peroxide and the strong alkalinity of the active material (pH $>$ 12 in aqueous solution), a control experiment was conducted under the same conditions (same amount of H_2O_2 and the calcination temperature) to evaluate the influence of hydrogen peroxide and labeled as H-NMCFO-X °C. Similarly, the materials from control experiments to understand the influence of calcination temperature were labeled as NMCFO-X °C. Additionally, different volumes of coating solution were applied to determine the optimal coating content relative to the amount of active material, 23.2 mL (2.5 wt.%) and 92.8 mL (10 wt.%), and were named as 2 wt.% Nb-NMCFO and 10 wt.% Nb-NMCFO.

Material Characterization

A scanning electron microscope SEM (Zeiss Supra 55) equipped with an energy-dispersive X-ray spectroscopy EDX (EDX Detector Apollo 40 SSD, EDAX Inc., USA) was used to analyze the morphology and elemental distribution. Cross-section electrode imaging with smooth surfaces were prepared via a broad-ion beam slope cutting (BIBSC) method with ion beam milling system Leica EM TIC 3X. Transmission electron microscopy (TEM) and scanning transmission electron microscopy (STEM) imaging was performed on a Thermo Fisher Talos F200i TEM. For EDX mapping, two Bruker DualX windowless EDX detectors and simultaneously acquired high-angle annular dark field (HAADF) and bright-field (BF) signals were used in STEM mode for imaging. Elemental mapping and quantification of the spectra was performed using the ThermoFisher Velox software with the Brown-Powell model for the ionization cross-sections. The samples were prepared by dispersing the powder on gold TEM grids with a lacey carbon support film. Powder X-ray diffraction was recorded using a Bruker D8 Phaser Diffractometer with Cu-K_α radiation (λ = 1.5406 Å) and a LynxEye XE-T detector in reflection mode. XRD patterns were recorded over a 2θ range of 10–80° with step size of 0.02° and counting time of 1s per step. Rietveld refinements were performed with TOPAS-V6 (Bruker AXS). X-ray photoelectron spectroscopy (XPS) was conducted on a K-Alpha XPS spectrometer (Thermo Fisher Scientific, Brno, Czech Republic) with a microfocused, monochromated Al K_α X-ray source (400 μm spot size). A glove box filled with Argon is directly attached to the spectrometer in order to avoid any air contact of the samples before analysis. Data acquisition and processing were conducted with the Thermo Avantage software. The K-Alpha charge compensation system was employed during analysis, using electrons of 8 eV energy, and low-energy argon ions to prevent any localized charge build-up. The spectra were fitted with one or more Voigt profiles (BE uncertainty: $\pm$ 0.2 eV) and Scofield sensitivity factors were applied for quantification.[36] All spectra were referenced to the C 1s peak (C—C, C—H) at 285.0 eV binding energy controlled by means of the well-known photoelectron peaks of metallic Cu, Ag, and Au, respectively. Inductively coupled plasma-optical emission spectroscopy (ICP-OES, iCAP 7600 Duo, Thermo Fisher Scientific) was applied to determine the chemical composition of processed materials. The specific surface area was measured via a Gemini VII 2390a (NSA, Micromeritics) and calculated with the Brunauer–Emmet–Teller (BET) method.

Electrochemical Measurements

The electrode slurry was prepared by mixing the active material, polyvinylidene fluoride (PVDF, Sigma–Aldrich), and carbon black (C-NERGY super C_{65}, Imerys Graphite, Bodio, Switzerland) in an 80:10:10 mass ratio using N-methyl-2-pyrrolidone (NMP) as the solvent. The mixture was homogenized in a Speedmixer (DAC S-150, Hauschild, Germany) at 2000 rpm for 5 min and 500 rpm for 3 min (degassing). The slurry was then coated onto the aluminum foil via a doctor blade coater (Erichsen Model 360, Germany) with a 200 μm gap height and a blade speed of 1.5 mm s^{-1} on the programmed coating device (Erichsen Coater 510, Germany). The coated electrodes were first dried in air at 80 °C for 30 min on the coater, then at 110 °C overnight under vacuum. After drying, the electrodes were punched into 12 mm discs and pressed with a hydraulic press with a force of 5 KN for 10 s and then transferred into an argon-filled glove box (H_2O and O_2 level $\leq$ 0.5 ppm, MBraun, Germany) for later battery assembly. The average active material mass loading is 3 – 4 mg cm^{-2}. The aqueous-processed hard carbon (HC) electrodes were also cast onto aluminum foil, following the detail fabrication procedure reported elsewhere.[37] CR 2032 coin-type half-cells were assembled in the glove box using aforementioned 12 mm diameter positive electrode, a 16.5 mm diameter glass fiber separator (Whatman GF/C), 120 μL of the POLiS reference electrolyte,[37] 13.5 mm diameter sodium metal chip as negative electrode, 1 mm stainless steel spacer, and stainless steel springer. The electrolyte composition consists of 1 M sodium hexafluorophosphate ($NaPF_6$) dissolved in a mixture of

ethylene carbonate/propylene carbonate (EC/PC, 1:1, wt.%) with 5 wt.% fluorethylencarbonate (FEC). Galvanostatic charge/discharge cycling test for half-cell measurements was performed on BT2000 Battery Cycler (Arbin Instruments, College Station, Texas, USA) and Biologic MPG-200 Potentiostat in a temperature-controlled room of 23 °C, following the standardized protocol of a 5 h resting period to reach a steady state, two formation cycles at 0.1C and then long-term cycling tests at 1C within a voltage range of 2.0–4.3 V versus Na^+/Na ($1C = 100\ mA\ g^{-1}$). Full cell tests were conducted with similar setup but using presodiated hard carbon electrodes within an enlarged voltage range of 1.5–4.2 V to understand the material degradation mechanism. The presodiation procedure of hard carbon electrodes was achieved by electrochemical cycling against sodium chip between 0.005 and 2 V for 5 cycles at 28 mA g^{-1} using same electrolyte and stopped at fully sodiated state, ensuring complete sodium intercalation. The electrodes were then disassembled, dried, and subsequently assembled into full cell with the prepared positive electrodes. High N/P values (2.6–3.0, depending on the positive electrode mass) here would be chosen to ensure that the presodiated hard carbon electrode could supply sufficient Na^+ during the battery cycling. Electrochemical impedance spectroscopy (EIS) measurements were performed on batteries at the fully charged state (4.2 V) on the same Biologic Potentiostat in a frequency range of 100 kHz to 10 mHz with an AC amplitude of 5 mV and the data were fitted using software RelaxIS3. For postmortem analysis, batteries cycled 200 times were disassembled in glovebox and electrodes were carefully washed with dimethyl carbonate (DMC) and dried for further characterization.

Acknowledgements

The authors thankfully acknowledged the support of Xuebin Wu (Institute for Applied Materials—Energy Storage Systems, Karlsruhe Institute of Technology) for manuscript reviewing, Monika Raab (Institute for Applied Materials—Energy Storage Systems, Karlsruhe Institute of Technology) for BET measurement, Dr. Anna Smith (Institute for Applied Materials—Energy Storage Systems, Karlsruhe Institute of Technology) for providing hard carbon electrode, Dr. Andreas Hofmann (Institute for Applied Materials—Materials Science and Engineering, Karlsruhe Institute of Technology) for electrolyte preparation, and Dr. Thomas Bergfeldt (Institute for Applied Materials—Applied Materials Physics, Karlsruhe Institute of Technology) for ICP-OES measurements. R.L. and S.F. acknowledge financial support from the German Federal Ministry of Research, Technology and Space (BMFTR) in the NanoMatFutur program (grant no. 03XP0423) and basic funding from the Helmholtz Association. This work contributes to the research performed at CELEST (Center for Electrochemical Energy Storage Ulm-Karlsruhe) and was funded by the German Research Foundation (DFG) under Project ID 390874152 (POLiS Cluster of Excellence, EXC 2154). Open Access funding enabled and organized by Projekt DEAL.

Conflict of Interest

The authors declare no conflict of interest.

Data Availability Statement

The original data are available on Zenodo (Link: https://zenodo.org/records/17949323), and the Supporting Information can be accessed via the Wiley Online Library.

Keywords: cycling stability · layered oxide cathodes · sodium-ion batteries · surface coating

[1] A. Rudola, A. J. R. Rennie, R. Heap, S. S. Meysami, A. Lowbridge, F. Mazzali, R. Sayers, C. J. Wright, J. Barker, *J. Mater. Chem. A.* **2021**, *9*, 8279.
[2] U.S. Geological Survey *Mineral commodity summaries* **2020**, https://pubs.usgs.gov/publication/mcs2020.
[3] C. Vaalma, D. Buchholz, M. Weil, S. Passerini, *Nat. Rev. Mater.* **2018**, *3*, 1.
[4] K. Kubota, S. Komaba, *J. Electrochem. Soc.* **2015**, *162*, A2538.
[5] Z. Song, Y. Liu, Z. Guo, Z. Liu, Z. Li, J. Zhou, W. Liu, R. Liu, J. Zhang, J. Luo, H. Jiang, J. Ding, W. Hu, Y. Chen, *Adv. Funct. Mater.* **2024**, *34*, 2313998.
[6] K. Kaliyappan, W. Xaio, T.-K. Sham, X. Sun, *Adv. Funct. Mater.* **2018**, *28*, 1801898.
[7] C. Delmas, C. Fouassier, P. Hagenmuller, *Physica B+C.* **1980**, *99*, 81.
[8] C. Fouassier, C. Delmas, P. Hagenmuller, *Mater. Res. Bull.* **1975**, *10*, 443.
[9] Y. Li, Z. Yang, S. Xu, L. Mu, L. Gu, Y.-S. Hu, H. Li, L. Chen, *Adv. Sci.* **2015**, *2*, 1500031.
[10] M. Malik, K. H. Chan, G. Azimi, *Mater. Today Energy* **2022**, *28*, 101066.
[11] Z. Ahaliabadeh, X. Kong, E. Fedorovskaya, T. Kallio, *J. Power Sources* **2022**, *540*, 231633.
[12] M. Schmidt, V. Mereacre, H. Geßwein, N. Bohn, S. Indris, J. R. Binder, *Adv. Energy Mater.* **2024**, *14*, 2301854.
[13] M. Häringer, H. Geßwein, N. Bohn, H. Ehrenberg, J. R. Binder, *ChemElectroChem* **2024**, *11*, e202300401.
[14] Y. Liu, X. Fang, A. Zhang, C. Shen, Q. Liu, H. A. Enaya, C. Zhou, *Nano Energy* **2016**, *27*, 27.
[15] V. Mereacre, P. Stüble, J. R. Binder, *Batteries Supercaps* **2025**, *8*, e202400666.
[16] J. H. Jo, H. J. Kim, J. U. Choi, N. Voronina, K.-S. Lee, K. Ihm, H.-K. Lee, H.-D. Lim, H. Kim, H.-G. Jung, K. Y. Chung, H. Yashiro, S.-T. Myung, *Energy Stor. Mater.* **2022**, *46*, 329.
[17] P. Yan, J. Zheng, J. Liu, B. Wang, X. Cheng, Y. Zhang, X. Sun, C. Wang, J.-G. Zhang, *Nat. Energy* **2018**, *3*, 600.
[18] B. N. Nunes, W. van den Bergh, F. Strauss, A. Kondrakov, J. Janek, T. Brezesinski, *Inorg. Chem. Front.* **2023**, *10*, 7126.
[19] H. Yu, S. Wang, Y. Hu, G. He, L. Q. Bao, I. P. Parkin, H. Jiang, *Green Energy Environ.* **2022**, *7*, 266.
[20] F. Xin, H. Zhou, Y. Zong, M. Zuba, Y. Chen, N. A. Chernova, J. Bai, B. Pei, A. Goel, J. Rana, F. Wang, K. An, L. F. J. Piper, G. Zhou, M. S. Whittingham, *ACS Energy Lett.* **2021**, *6*, 1377.
[21] S. Lavela, A. C. do N. Santos, F. V. da Motta, M. R. D. Bomio, P. Lavela, C. Pérez Vicente, J. L. Tirado, *ACS Appl. Mater. Interfaces* **2024**, *16*, 56975.
[22] N. Yabuuchi, M. Takeuchi, M. Nakayama, H. Shiiba, M. Ogawa, K. Nakayama, T. Ohta, D. Endo, T. Ozaki, T. Inamasu, K. Sato, S. Komaba, *Proc. Natl. Acad. Sci. U.S.A.* **2015**, *112*, 7650.
[23] C. Nico, T. Monteiro, M. P. F. Graça, *Prog. Mater. Sci.* **2016**, *80*, 1.
[24] Y. Zhou, M. Sun, M. Cao, Y. Zeng, M. Su, A. Dou, X. Hou, Y. Liu, *J. Colloid Interface Sci.* **2024**, *657*, 472.
[25] M. Linz, F. Bühner, D. Paulus, L. Hennerici, Y. Guo, V. Mereacre, U. Mansfeld, M. Seipenbusch, J. Kita, R. Moos, *Adv. Mater.* **2024**, *36*, 2308294.
[26] V. Mereacre, P. Stüble, V. Trouillet, S. Ahmed, K. Volz, J. R. Binder, *Adv. Mater. Interfaces* **2023**, *10*, 2201324.
[27] J. C. Garcia, J. Bareño, J. Yan, G. Chen, A. Hauser, J. R. Croy, H. Iddir, *J. Phys. Chem. C.* **2017**, *121*, 8290.
[28] J. Xu, J. Chen, K. Zhang, N. Li, L. Tao, C.-P. Wong, *Nano Energy* **2020**, *78*, 105142.
[29] L. F. Pfeiffer, M. Dillenz, N. Burgard, P. Beran, D. Roscher, M. Zarrabeitia, P. Drews, C. Hervoches, D. Mikhailova, A. Omar, V. Baran, N. Paul, M. Sotoudeh, M. Busch, M. Wohlfahrt-Mehrens, A. Groß, S. Passerini, P. Axmann, *J. Mater. Chem. A.* **2025**, *13*, 540.
[30] L. Pauling, *J. Am. Chem. Soc.* **1929**, *51*, 1010.
[31] M. Toupin, T. Brousse, D. Bélanger, *Chem. Mater.* **2002**, *14*, 3946.

[32] Y. Wang, J. Jin, X. Zhao, Q. Shen, X. Qu, L. Jiao, Y. Liu, *Angew. Chem., Int. Ed.* **2024**, *63*, e202409152.
[33] T. Zhang, M. Ren, Y. Huang, F. Li, W. Hua, S. Indris, F. Li, *Angew. Chem., Int. Ed.* **2024**, *63*, e202316949.
[34] X. Chen, L. Li, M. Liu, T. Huang, A. Yu, *J. Power Sources* **2021**, *496*, 229867.
[35] J. Fondard, E. Irisarri, C. Courrèges, M. R. Palacin, A. Ponrouch, R. Dedryvère, *J. Electrochem. Soc.* **2020**, *167*, 070526.
[36] J. H. Scofield, *J. Electron Spectrosc. Relat. Phenom.* **1976**, *8*, 129.
[37] P. Stüble, C. Müller, N. Bohn, M. Müller, A. Hofmann, T. Akçay, J. Klemens, A. Koeppe, S. Kolli, D. Rajagopal, H. Geßwein, W. Schabel, P. Scharfer, M. Selzer, J. R. Binder, A. Smith, *Batteries Supercaps* **2024**, *7*, e202400406.
[38] J.-F. Bérar, P. Lelann, *J. Appl. Crystallogr.* **1991**, *24*, 1.

Manuscript received: August 28, 2025
Revised manuscript received: November 14, 2025